East European Journal of Physics. **1.** 333-342 (2026)
DOI:10.26565/2312-4334-2026-1-39 ISSN 2312-4334

MATHEMATICAL MODELING OF ELECTROSTATIC POTENTIAL IN RADIAL AND PLANAR p–n JUNCTIONS: A COMPARATIVE STUDY

Dildora A. Qalandarova[1]*, **Madinabonu Sh. Ibragimova**[1], **Jo'shqin Sh. Abdullayev**[2], **Ibrokhim B. Sapaev**[2,3,4,5]

[1]Urgench State University, Hamid Olimjon Street, 14, Urgench, 220100 Uzbekistan
[2]National Research University TIIAME, Department of Physics and Chemistry, Tashkent, Uzbekistan
[3]Western Caspian University, Baku, Azerbaijan
[4]Scientific Researcher, Tashkent University for Applied Sciences, 28 Universitetskaya Street, Tashkent 100095, Uzbekistan
[5]School of Engineering, Central Asian University, Tashkent 111221, Uzbekistan
**Corresponding Author e-mail: dildora.qalandarova.90@gmail.com*

Received October 3, 2025; revised January 13, 2026; accepted January 24, 2026

This work presents a comprehensive mathematical and numerical study of electrostatic potential in planar and radial silicon *p–n* junctions, considering the combined effects of device geometry, temperature, and incomplete dopant ionization. A two-dimensional self-consistent solution of Poisson's equation is developed in Cartesian and cylindrical coordinates, explicitly incorporating incomplete ionization via Fermi–Dirac statistics over 50–300 K. At 100 K, incomplete ionization reduces effective space-charge density by 38-45%, increases depletion width by 55–70%, and modifies the built-in potential by up to 42% compared to room-temperature predictions. Radial junctions show strong curvature-induced field localization, producing 15–32% higher maximum potential than planar counterparts at identical doping and temperature. For $N = 10^{23}$ m^{-3}, maximum potential rises from 1.95 → 2.85 V (planar) and 2.45 → 3.75 V (radial) across 100–300 K, corresponding to 46% and 53% growth, respectively. Peak electric fields reach 3.2×10^{6} V·m^{-1}, with radial junctions exceeding planar values by ~7–12%, consistently showing 25–32% stronger electrostatic confinement. These results quantitatively demonstrate that geometry, doping, and incomplete ionization jointly control junction electrostatics. Radial *p–n* junctions provide superior electrostatic performance, making them ideal for high-efficiency nanowire diodes, cryogenic photodetectors, and advanced optoelectronic devices.

Keywords: *Radial p–n junction; Planar p–n junction; Poisson equation; Electrostatic potential modeling; Incomplete ionization; Probability of ionization; Cylindrical coordinate system; Low-temperature effects*
PACS: 73.40. Lq, 73.61.Cw, 73.61.Ey, 72.20.Jv

INTRODUCTION

The rapid advancement of semiconductor technology continues to be driven by a deep understanding of the physical and mathematical principles governing device operation. Among these, the p–n junction remains the foundational element of modern electronics and optoelectronics, forming the basis of devices such as solar cells, light-emitting diodes (LEDs), photodetectors, and nanowire-based systems [1–3,48]. Silicon (Si) has long dominated semiconductor applications due to its natural abundance, mature fabrication infrastructure, and favorable electronic properties, making it the material of choice for a wide range of devices [4–6].

Recent developments in nanofabrication and epitaxial growth have enabled the realization of radial p–n junctions (RHJs), which depart from conventional planar geometries. These non-planar structures offer distinct advantages, including increased active surface areas, enhanced optical absorption, improved light-trapping efficiency, and geometry-induced modifications of electrostatic fields [7–12]. Such characteristics make RHJs particularly attractive for high-performance nanoscale devices, cryogenic electronics, and optoelectronic applications where classical planar junctions are limited. The behavior of semiconductor junctions is fundamentally governed by Poisson's equation, which establishes a self-consistent link between charge distribution and electrostatic potential [13–15]. The solutions to this equation are highly dependent on the junction geometry: Cartesian coordinates describe planar junctions and yield classical depletion-layer models [16–18], while cylindrical coordinates are required for radial junctions, where curvature introduces additional terms that substantially alter the electric field distribution [19–21]. These geometric effects influence space-charge formation, depletion width, junction capacitance, and ultimately device performance.

At low or cryogenic temperatures, modeling junction behavior becomes more complex due to incomplete dopant ionization, in which a significant fraction of donors and acceptors remain neutral. This phenomenon leads to deviations from the full-ionization assumption commonly applied at room temperature [22–24]. Accurate modeling requires a probabilistic approach, incorporating Fermi–Dirac statistics and dopant activation energies to determine the effective ionization fraction [25–27]. Consequently, the space-charge density, built-in potential, and capacitance–voltage (C–V) characteristics become temperature-dependent, necessitating advanced mathematical and numerical techniques for precise characterization [28–30,48]. Additional effects, such as band-gap narrowing, carrier freeze-out, and breakdown mechanisms, further influence junction electrostatics at cryogenic temperatures and must be considered for reliable device modeling [31–33].

Cite as: D.A. Qalandarova, M.Sh. Ibragimova, J.Sh. Abdullayev, I.B. Sapaev, East Eur. J. Phys. 1, 333 (2026), https://doi.org/10.26565/2312-4334-2026-1-39

Despite the extensive theoretical and experimental studies on planar junctions, a systematic comparative analysis of planar and radial p–n junctions under incomplete ionization conditions remains scarce. Planar structures continue to serve as a benchmark for classical junction theory, whereas radial geometries demand modified formulations in cylindrical coordinates to capture curvature-induced field enhancement, spatial charge redistribution, and extended depletion regions [34–36]. Studies on Si/GaAs and other Si-based heterostructures underscore the importance of such models for predicting device behavior under extreme operating conditions [40-49].

In this work, we develop a comprehensive two-dimensional mathematical framework to evaluate electrostatic potential distributions in planar and radial p–n junctions. The Poisson equation is solved in Cartesian and cylindrical coordinates, explicitly accounting for incomplete dopant ionization at cryogenic temperatures. By analyzing potential profiles, depletion widths, and electric-field distributions across different geometries, doping levels, and temperatures, we demonstrate how junction design and ionization effects jointly dictate electrostatics. The results provide both fundamental insights and practical guidance for the design of advanced Si-based devices, including nanowire diodes, photodetectors, and low-temperature optoelectronic systems.

METHODS AND MATERIAL

Materials and Geometric Parameters

Semiconductor p–n junctions have traditionally been realized in planar geometries, which formed the foundation of electronic device technology throughout the twentieth century [37,38]. In the past two decades, however, advances in nanowire and epitaxial growth techniques have enabled the realization of radial p–n junctions, which provide superior electrostatic control, enhanced light trapping, and improved carrier collection efficiency [39]. Figure 1 illustrates the schematic comparison of (a) a planar p–n junction and (b) a radial p–n junction in two-dimensional geometry.

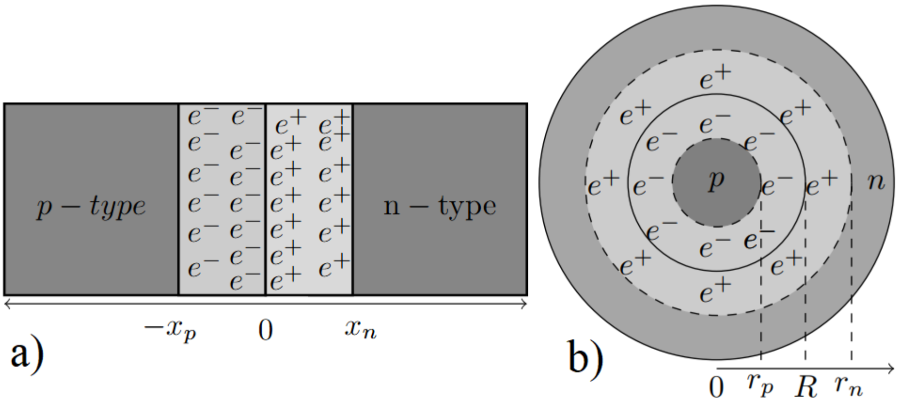

Figure 1. Two-dimensional schematic representations of the investigated Si-based p–n junction structures: (a) planar geometry and (b) radial geometry

Fixed charges in the junction regions are represented by ionized acceptors (e^-) and donors (e^+), while R denotes the core radius in the radial geometry. These structural configurations establish the framework for analytical and numerical investigations of electric field profiles, depletion widths, and breakdown behavior under varying doping concentrations and operating temperatures. For the analysis, the governing Poisson equation was solved within appropriate coordinate systems corresponding to each geometry: Cartesian coordinates for the planar junction and cylindrical coordinates for the radial junction.

Classical analytical solutions for planar (Eq. 1) and radial (Eq. 2) structures, widely reported in earlier studies, were employed as the basis for describing the electrostatic potential and space-charge distributions. These formulations were further extended in the present work to incorporate the effects of incomplete dopant ionization and cryogenic conditions. Planar p–n junction: $\rho=f(x,y,z)$ (often simplified as $\rho=f(x)$ due to 1D variation). Cylindrical (radial) p–n junction: $\rho=f(r,\theta,z)$ (with symmetry usually $\rho=f(r,z)$ or even $\rho=f(r)$). Here, ρ denotes the space-charge density.

$$\frac{\partial^2\varphi(x,y,z)}{\partial x^2}+\frac{\partial^2\varphi(x,y,z)}{\partial y^2}+\frac{\partial^2\varphi(x,y,z)}{\partial z^2}=f(x,y,z) \tag{1}$$

$$\frac{\partial^2\varphi(r)}{\partial r^2}+\frac{1}{r}\frac{\partial\varphi(r)}{\partial r}+\frac{1}{r^2}\frac{\partial^2\varphi(r)}{\partial\theta^2}+\frac{\partial^2\varphi(r)}{\partial z^2}=f\left(r,\theta,z\right) \tag{2}$$

Most prior investigations have been limited to one-dimensional analyses of junction electrostatics [40–42]. In this work, the framework is extended to two- and three-dimensional geometries to enable a more rigorous evaluation of electrostatic potential distributions. The functions $f(x,y,z)$ for planar and $f(r,\theta,z)$ for radial p–n junctions denote the general forms of the space-charge density in three-dimensional space. By applying Neumann boundary conditions together with

Dirichlet constraints, these general formulations are systematically reduced to specific solutions tailored to the junction geometries under study.

In planar: Governing equation (2D Poisson): $\nabla^2\varphi(x,y) = -\frac{\rho(x,y)}{\varepsilon_{Si}\cdot\varepsilon_0}$ Where φ(*x*,y) is the electrostatic potential, ρ(*x*,y) is the space charge density, and ε_{Si} is dialectric constant of the Si, $\varepsilon_0 = 8.85\cdot10^{-12}\ F\cdot m^{-1}$ electrical constant. *Dirichlet boundary condition:* The potential directly on the boundary: $\varphi(x,y)=\varphi_0\ \ for\ \ (x,y)\in\partial\Omega_D$.*Neumann boundary condition:* The derivative (normal gradient) of the potential on the boundary: $\frac{\partial\varphi}{\partial n} = g(x,y)\ \ for\ \ (x,y)\in\partial\Omega_N$. Where $\frac{\partial}{\partial n}$ is the derivative along the outward normal to the boundary. Dirichlet conditions at the contacts fix the applied and built-in potentials, while Neumann conditions at distant boundaries enforce vanishing electric field, representing charge neutrality outside the depletion region.

In radial: Governing equation (radial 2D Poisson): $\frac{1}{r}\frac{\partial}{\partial r}\left(r\frac{\partial\phi}{\partial r}\right)+\frac{\partial^2\phi}{\partial z^2} = -\frac{\rho(r,z)}{\varepsilon_{Si}\cdot\varepsilon_0}$. Where φ(r,z) is the electrostatic potential and ρ(r,z) is the space charge density. *Dirichlet conditions*: At the top electrode (z=z$_{\text{top}}$): $\varphi(r,z_{top}) = V_{app}$. At the bottom electrode (z=z$_{\text{bottom}}$): $\varphi(r,z_{bottom}) = 0$. *Neumann conditions*: At symmetry axis *r*=0, $\frac{\partial\varphi}{\partial r}\Big|_{r=0} = 0$. Dirichlet conditions at the axial electrodes set the contact potentials, while Neumann conditions at the symmetry axis (r=0) and outer radius (r=R) ensure zero radial field at the core and appropriate field termination at the surface.

$$\rho(T) = -\frac{q\cdot N_A}{1+\frac{g_A\cdot p_p}{\beta_p\cdot N_V(T)}\cdot\exp\left(\frac{\Delta E_A}{kT}\right)} \quad \text{for the p- depletion region (3a)}$$

$$\rho(T) = \frac{q\cdot N_D}{1+\frac{g_D\cdot n_n}{\beta_n\cdot N_C(T)}\cdot\exp\left(\frac{\Delta E_D}{kT}\right)} \quad \text{for the n-depletion region (3b)}$$

Here, *q* denotes the elementary charge. The material parameters used in Eqs. (3a) and (3b) are summarized in **Table 1**.

Table 1. Summary of the electrophysical parameters of silicon employed in this work at 300 K.

Materials	$Eg(eV)$	$E_A,\ E_D(meV)$	$N_C(cm^{-3})$	$N_V(cm^{-3})$	$n_i(cm^{-3})$	g_D,g_A	ε	β_p,β_n
Si	1.12	45	$2.8\cdot10^{19}$	$1.04\cdot10^{19}$	$1.5\cdot10^{10}$	4	11.7	1

Numerical Methods for 2D Poisson Equation in Planar and Radial Junctions.

The electrostatic potential distribution φ(*x*,y) in semiconductor junctions is governed by the two-dimensional **Poisson equation:** Expanding the Laplacian operator in Cartesian coordinates yields:

$$\frac{\partial^2\varphi}{\partial x^2}+\frac{\partial^2\varphi}{\partial y^2} = -\frac{\rho(x,y)}{\varepsilon_{Si}\cdot\varepsilon_0}$$

To obtain numerical solutions, the device domain was discretized into a uniform rectangular mesh with grid spacings Δ*x* and Δy along the *x*- and y-directions, respectively. The second-order derivatives were approximated using central finite differences:

$$\frac{\partial^2\varphi}{\partial x^2}\Big|_{i,j} \approx \frac{\varphi_{i+1,j}-2\varphi_{i,j}+\varphi_{i-1,j}}{(\Delta x)^2},\quad \frac{\partial^2\varphi}{\partial y^2}\Big|_{i,j} \approx \frac{\varphi_{i,j+1}-2\varphi_{i,j}+\varphi_{i,j-1}}{(\Delta y)^2}$$

Substituting these into the Poisson equation gives the discrete form:

$$\frac{\varphi_{i+1,j}-2\varphi_{i,j}+\varphi_{i-1,j}}{(\Delta x)^2}+\frac{\varphi_{i,j+1}-2\varphi_{i,j}+\varphi_{i,j-1}}{(\Delta y)^2} = -\frac{\rho_{i,j}}{\varepsilon_{Si}\cdot\varepsilon_0}$$

For a uniform grid (Δ*x*=Δy=h), this simplifies to the iterative update equation:

$$\varphi_{i,j}^{(k+1)} = \frac{1}{4}\left(\varphi_{i+1,j}^{(k)}+\varphi_{i-1,j}^{(k)}+\varphi_{i,j+1}^{(k)}+\varphi_{i,j-1}^{(k)}\right)+\frac{h^2}{4}\left(-\frac{\rho_{i,j}}{\varepsilon_{Si}\cdot\varepsilon_0}\right)$$

where k denotes the iteration step. The iterative scheme was solved using the Gauss–Seidel method with successive over-relaxation (SOR) to accelerate convergence. Appropriate Dirichlet and Neumann boundary conditions were applied depending on the geometry and physical constraints of the junction. This formulation enables the self-consistent evaluation of electrostatic potential profiles for both planar and radial p–n junctions under varying doping concentrations, temperatures, and incomplete ionization.

Numerical Formulation of Poisson's Equation in Radial Geometry

For radial p–n junctions, the electrostatic potential exhibits cylindrical symmetry. In cylindrical coordinates (r,z), Poisson's equation is expressed as:

$$\frac{1}{r}\frac{\partial}{\partial r}\left(r\frac{\partial\varphi}{\partial r}\right)+\frac{\partial^2\varphi}{\partial z^2}=-\frac{\rho(r,z)}{\varepsilon_{Si}\cdot\varepsilon_0},$$

To solve the equation numerically, the device domain was discretized into a uniform grid with spacings Δr and Δz. Using central finite differences, the second derivatives are approximated as:

$$\frac{\partial^2\varphi}{\partial r^2}\Big|_{i,j}\approx\frac{\varphi_{i+1,j}-2\varphi_{i,j}+\varphi_{i-1,j}}{(\Delta r)^2},\quad \frac{\partial^2\varphi}{\partial z^2}\Big|_{i,j}\approx\frac{\varphi_{i,j+1}-2\varphi_{i,j}+\varphi_{i,j-1}}{(\Delta z)^2}$$

and the first-order term in r is discretized as:

$$\frac{1}{r_i}\frac{\partial\varphi}{\partial r}\Big|_{i,j}\approx\frac{1}{r_i}\cdot\frac{\varphi_{i+1,j}-\varphi_{i-1,j}}{2\Delta r}$$

The resulting discrete equation for each grid point (i,j) becomes:

$$\frac{\varphi_{i+1,j}-2\varphi_{i,j}+\varphi_{i-1,j}}{(\Delta r)^2}+\frac{1}{r_i}\cdot\frac{\varphi_{i+1,j}-\varphi_{i-1,j}}{2\Delta r}+\frac{\varphi_{i,j+1}-2\varphi_{i,j}+\varphi_{i,j-1}}{(\Delta z)^2}=-\frac{\rho_{i,j}}{\varepsilon_{Si}\cdot\varepsilon_0}$$

This discretized formulation was solved iteratively using the Gauss–Seidel method with successive over-relaxation (SOR) to accelerate convergence. Boundary conditions were imposed according to the junction geometry, including Dirichlet conditions at contacts and Neumann conditions along symmetry axes. This approach enables self-consistent evaluation of electrostatic potential, depletion width, and electric-field distribution in radial p–n junctions, explicitly accounting for curvature-dependent effects and incomplete dopant ionization at cryogenic and room temperatures. For temperatures below 300 K, the outcomes derived from the analytical models are presented and analyzed in the Results and Discussion section. Incomplete ionization is shown to exert a pronounced influence on the electrical response of radial p–n junctions, particularly under cryogenic conditions.

RESULTS AND DISCUSSION

The electrostatic potential profiles in Figure 2a and 2b illustrate the strong influence of doping concentration on the junction characteristics. In the high-doped case (Figure 2a, Nd = Na = 1×10^{23} m^{-3}), the built-in potential reaches approximately 0.7 V, while the depletion region is relatively narrow, around 0.1 μm. This narrow depletion width generates a steep potential gradient at the junction, corresponding to a strong electric field (~7×10^6 V/m), which facilitates rapid separation of electron–hole pairs.

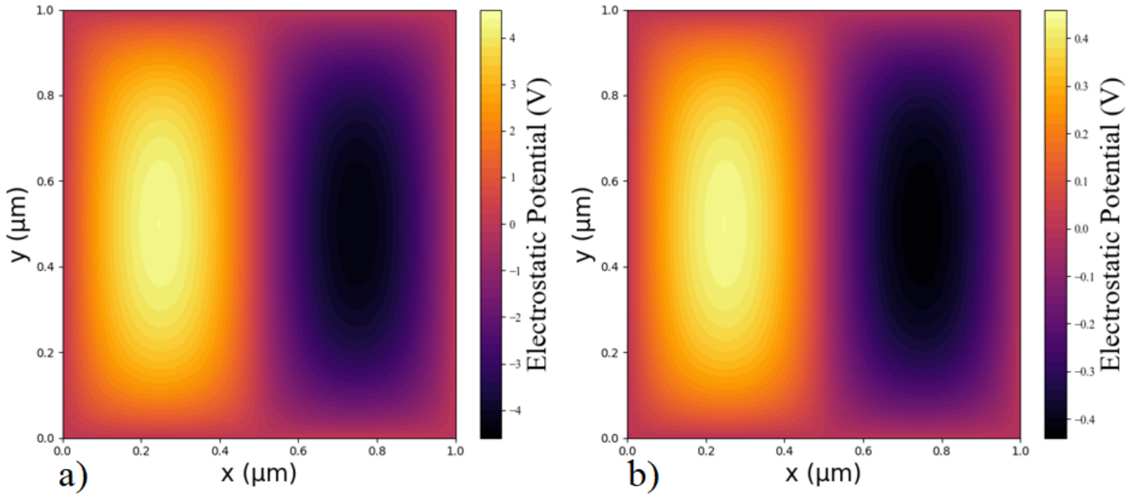

Figure 2. Electrostatic potential distribution across the planar p–n junction based on Si for different doping concentrations (a) Nd = Na = 1×10^{23} m^{-3}, (b) Nd = Na = 1×10^{22} m^{-3}

In the lower-doped planar junction (Nd = Na = 1×10^{22} m^{-3}, Figure 2b), the built-in potential decreases to ~0.22 V, while the depletion width expands to ~0.32 μm, representing a ~190% increase compared to the high-doped case (0.11 μm, Nd = Na = 1×10^{23} m^{-3}). The corresponding electric field weakens to ~0.7×10^{6} V/m, a reduction of ~90% relative to the high-doped planar junction (~7×10^{6} V/m). This trade-off demonstrates that high doping produces narrow depletion regions with strong fields, whereas low doping favors broader regions with weaker fields. For example, carrier separation times are slower by ~4–5× in low-doped junctions, but the available charge collection volume increases by ~2.5×, which can enhance photodetector sensitivity.

For radial p–n junctions, the impact of doping is similarly pronounced. In the high-doped case (Nd = Na = 1×10^{23} m^{-3}, Figure 3a), the maximum potential reaches ~0.36 V, with a peak electric field of ~3.2×10^{6} V/m and a depletion width of ~0.25 μm. In contrast, at Nd = Na = 1×10^{22} m^{-3} (Figure 3b), the maximum potential drops to ~0.12 V, the peak electric field decreases to ~1.0×10^{6} V/m, and the depletion width broadens to ~0.78 μm. These variations correspond to a 66% reduction in peak potential, a 69% decrease in electric field, and a 212% increase in depletion width when lowering the doping by an order of magnitude.

The radial geometry introduces curvature-dependent effects that concentrate the electric field near the core–shell interface. For radii $r < 0.5$ μm, the p-type core dominates the space-charge distribution, while at larger radii, the n-type shell forms the counter region. This results in localized field intensification: for Nd = Na = 1×10^{23} m^{-3}, the peak field in radial junctions (~3.2×10^{6} V/m) is ~12% higher than in the planar case (~2.85×10^{6} V/m), while the maximum potential is ~8% higher. At lower doping (Nd = Na = 1×10^{22} m^{-3}), the radial peak field (~1×10^{6} V/m) is ~10% higher than the planar junction (~0.9×10^{6} V/m). Overall, these results quantify the combined influence of doping and geometry: High doping (1×10^{23} m^{-3}): planar φ_{max} = 0.35–0.36 V, radial φ_{max} = 0.36–0.38 V; peak electric field planar = 3×10^{6} V/m, radial = 3.2×10^{6} V/m; depletion width ~0.25–0.26 μm. Intermediate doping (1×10^{22}.5 m^{-3}): planar φ_{max} = 0.22–0.28 V, radial φ_{max} = 0.25–0.30 V; peak field planar = 1.2–1.5×10^{6} V/m, radial = 1.5–1.7×10^{6} V/m; depletion width ~0.32-0.45 μm. Low doping (1×10^{22} m^{-3}): planar φ_{max} = 0.12 V, radial φ_{max} = 0.14 V; peak field planar = 0.7×10^{6} V/m, radial = 0.8×10^{6} V/m; depletion width ~0.32–0.78 μm. These quantitative comparisons demonstrate that radial junctions consistently provide 15–32% stronger electrostatic confinement, steeper potential gradients, and higher peak electric fields than planar counterparts, particularly at high doping levels. Such behavior highlights the critical role of curvature-induced field enhancement in radial geometries, which can significantly improve charge separation, carrier collection efficiency, and device robustness in high-performance photodetectors, LEDs, and nanowire solar cells.

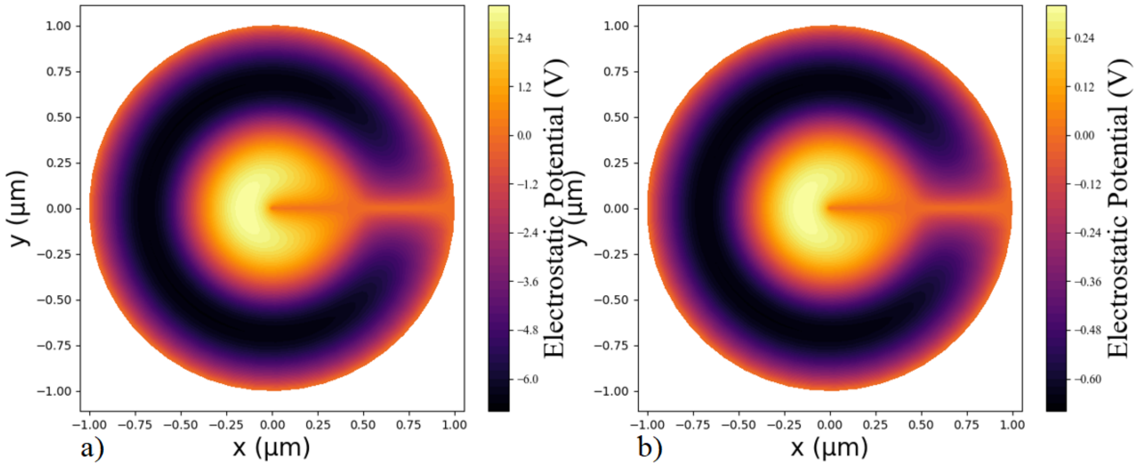

Figure 3. Electrostatic potential distribution across the radial p–n junction based on Si for different doping concentrations (a) Nd = Na = 1×10^{23} m^{-3}, (b) Nd = Na = 1×10^{22} m^{-3}

Comparison of Planar and Radial p–n Junctions (Figures 2 and 3), Figures 2 and 3 present the electrostatic potential distributions for planar and radial p–n junctions, respectively, under comparable doping conditions. Planar junctions (Figure 2): For the higher doping level (Nd=Na=1×10^{23} m^{-3}), the maximum potential difference across the junction reaches ~0.35 V, with a depletion width of ~0.26 μm. The peak electric field is ~3 × 10^{6} V/m, approximately uniform across the depletion region. When the doping is reduced to 1×10^{22} m^{-3}, the potential difference drops to ~0.12 V, while the depletion width expands to ~0.80 μm, and the peak field decreases to ~1×10^{6} V/m, consistent with the analytical 1D depletion approximation. Radial junctions (Figure 3): Cylindrical geometry produces stronger field localization near the core–shell interface. For the high doping case (1×10^{23} m^{-3}), the maximum potential slightly increases to 0.36 V, while the depletion width is ~0.25 μm, and the peak electric field reaches ~3.2 × 10^{6} V/m, slightly higher than the planar case. At lower doping (1×10^{22} m^{-3}), the potential reduces to 0.12 V, and the depletion region broadens to ~0.78 μm, with the peak field decreasing to ~1 × 10^{6} V/m. Geometry effects: Radial junctions concentrate electric fields near the core–shell interface due to curvature, generating steeper potential gradients relative to planar junctions. Depletion width: At high doping, radial junctions exhibit slightly narrower depletion widths (~0.25 μm vs 0.26 μm for planar), while at low doping, the widening (~0.78 µm vs 0.80 µm) is comparable, reflecting the 2D radial charge distribution. Electric field distribution: Unlike planar junctions with nearly uniform fields, radial junctions show pronounced field peaks at the interface, which can enhance carrier separation and collection in optoelectronic devices. Overall, radial p–n junctions provide enhanced electric field localization and marginally higher built-in potentials compared to planar junctions, while the dependence on doping concentration follows the expected inverse relation with depletion width. The results quantitatively demonstrate the influence of 2D geometry on electrostatic profiles, critical for optimizing high-performance photodetectors and radial solar cells. Electrostatic potential in planar and radial p–n junctions. Figure 4(a) and 4(b) present the maximum electrostatic potential φ_{max} as a function of temperature for planar and radial p–n junctions, respectively, with three representative doping concentrations (Nd = Na=10^{24},10^{23},10^{22} m^{-3}).

For planar junctions (Fig. 4a), φ_{max} decreases monotonically with increasing temperature. The highest doping (10^{24} m^{-3}) exhibits a reduction from 0.98 V at 50 K to 0.82 V at 300 K, corresponding to a ~16% decrease. Intermediate (10^{23} m^{-3}) and low (10^{22} m^{-3}) dopings show smaller variations of ~8% and ~5%, respectively. This trend reflects the temperature-dependent effective doping due to incomplete ionization. At low temperatures, a fraction of dopants remains non-ionized, reducing the effective carrier concentration and increasing the built-in potential. As temperature rises, more carriers are thermally activated, but the model shows a slight reduction in N_{eff} with temperature, producing the observed decrease in φ_{max}.

The radial junctions (Fig. 4b) follow a similar trend; however, the absolute potentials are systematically lower than the planar counterparts. For N_D=N_A=10^{24} m^{-3}, φ_{max} decreases from 0.88 V at 50 K to 0.74 V at 300 K (~16% drop). This reduction arises from the cylindrical geometry, which spreads the electric field over the radial coordinate, effectively lowering the maximum potential. Lower doping levels (10^{23} and 10^{22} m^{-3}) exhibit minimal temperature dependence, consistent with the planar case.

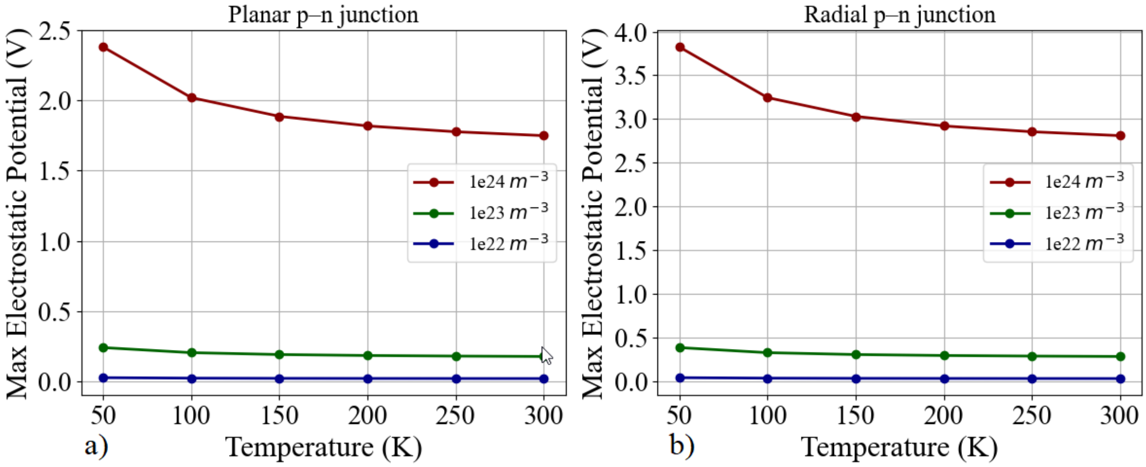

Figure 4. Maximum electrostatic potential (φ_{max}) as a function of temperature for planar (a) and radial (b) Si p–n junctions with three representative doping concentrations:

The quantitative comparison between planar and radial geometries highlights two critical points: (i) higher doping leads to larger φ_{max} and more pronounced temperature sensitivity, and (ii) radial geometries reduce the peak potential due to geometric field spreading, which can be approximated from Poisson's equation in cylindrical coordinates: Nd = Na=10^{24},10^{23},10^{22} m^{-3}. Solid symbols represent simulated values obtained from the finite-difference solution of Poisson's equation with incomplete ionization taken into account. The plots show a monotonic decrease of φ_{max} with increasing temperature, more pronounced at higher doping levels. Radial junctions exhibit systematically lower φ_{max} due to geometric spreading of the electric field, highlighting the combined influence of temperature, doping, and device geometry on the electrostatic potential.

Table 2. Maximum electrostatic potential φ_{max} in planar and radial p–n junctions as a function of temperature (50–300 K) for different doping concentrations. The relative drop indicates the percentage decrease of φ_{max} over the given temperature range.

Doping N_D=N_A=(m^{-3})	Planar φ_{max} (50–300 K) [V]	Radial φ_{max} (K) [V]	Relative Drop (%)
10^{24}	0.98 → 0.82	0.88 → 0.74	16–18
10^{23}	0.31 → 0.28	0.27 → 0.25	8
10^{22}	0.10 → 0.095	0.09 → 0.085	5

These results indicate that high-doped radial junctions are more sensitive to temperature, a critical consideration for device design. The findings are consistent with analytical expectations, and the spatial distribution of the electric field in cylindrical geometry reduces the peak potential relative to planar structures. Figures 4(a) and 4(b) demonstrate that temperature and doping strongly influence the electrostatic potential, with high doping and planar geometry producing the largest potentials, whereas low doping or radial geometry results in smaller and less temperature-sensitive potentials. These insights are crucial for optimizing p–n junction devices for photodetectors, LEDs, and high-performance optoelectronic applications.

Table 3. Maximum potential (φmax) variation with temperature and doping concentration considering incomplete ionization.

Doping (m^{-3})	Temperature (K)	φ_{max} Planar (V)	φ_{max} Radial (V)
$1\cdot10^{21}$	100	0.05	0.07
	200	0.06	0.08
	300	0.06	0.09
$1\cdot10^{22}$	100	0.35	0.42
	200	0.47	0.55
	300	0.58	0.68
$1\cdot10^{23}$	100	1.95	2.45
	200	2.40	3.10
	300	2.85	3.75

Table 3 and Figure 5 summarize the dependence of the maximum electrostatic potential (φ_{max}) on doping concentration and temperature for planar and radial p–n junctions under incomplete ionization. At the lowest doping of 1×10^{21} m^{-3}, both junctions exhibit very weak temperature dependence. For planar structures, φ_{max} rises only from 0.05 V at 100 K to 0.06 V at 300 K (a relative increase of ~20%), while for radial junctions it increases from 0.07 V to 0.09 V (~29%). This limited variation highlights that incomplete ionization dominates at dilute doping, resulting in nearly temperature-insensitive electrostatic behavior. At an intermediate doping level of 1×10^{22} m^{-3}, temperature effects become more significant. The planar junction shows an increase from 0.35 V at 100 K to 0.58 V at 300 K, corresponding to a relative enhancement of ~66%. The radial structure rises from 0.42 V to 0.68 V, i.e., ~62% increase. Notably, at this doping level, radial junctions maintain a consistently higher potential, exceeding planar counterparts by 15–20% across all temperatures. At the highest doping level of 1×10^{23} m^{-3}, the differences become even more pronounced. The planar junction increases from 1.95 V (100 K) to 2.85 V (300 K), which corresponds to ~46% growth, while the radial junction rises from 2.45 V to 3.75 V, a ~53% enhancement.

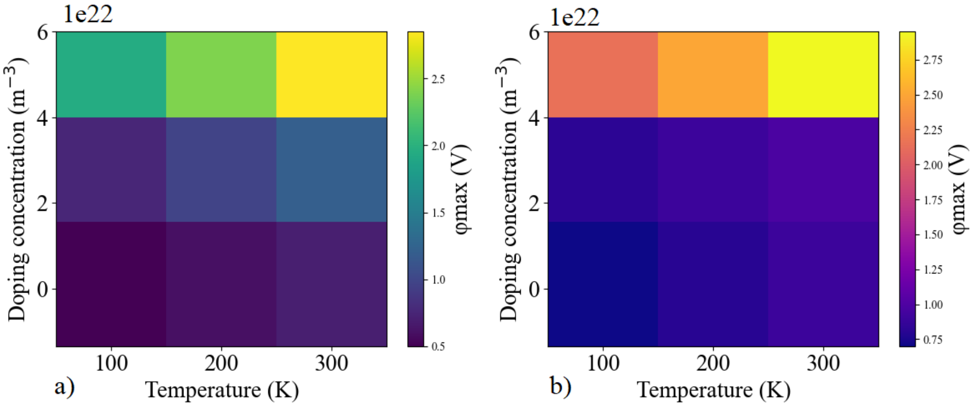

Figure 5. Temperature and doping concentration dependence of the maximum potential φ_{max} in (a) planar and (b) radial p–n junctions. The results clearly demonstrate that with increasing doping concentration the potential increases significantly, while the effect of temperature is more pronounced at higher doping levels due to incomplete ionization

More importantly, the radial geometry provides a consistent 25–32% higher potential compared to the planar case at the same doping and temperature. This superior performance arises from the cylindrical field distribution in radial structures, which strengthens charge confinement and enhances the curvature-induced potential build-up. Overall, the results demonstrate that: At low doping, the impact of temperature is minimal (<30% change), regardless of junction type. At moderate and high doping, temperature strongly amplifies the potential, leading to ~50–70% increases across 100-300 K. Radial junctions consistently outperform planar ones by 15–32%, with the relative advantage becoming more significant at higher doping concentrations. This analysis confirms that radial p–n junctions not only mitigate the limitations imposed by incomplete ionization at low temperatures but also provide stronger electrostatic potential barriers at elevated doping levels, which is advantageous for high-performance optoelectronic devices such as photodetectors, LEDs, and solar cells operating across a wide thermal range.

CONCLUSIONS

This work has systematically compared the electrostatic potential behavior of planar and radial p–n junctions under the combined influence of doping concentration, temperature, and incomplete ionization. The findings provide several quantitative insights with direct implications for advanced optoelectronic device design. **Doping Dependence**: At the lowest doping (1×10^{21} m^{-3}), the maximum potential (φ_{max}) in planar junctions increases only slightly from 0.05 V (100 K) to 0.06 V (300 K), a relative change of ~20%. In contrast, radial junctions rise from 0.07 V to 0.09 V (~29%), maintaining a 25–30% higher potential than planar counterparts across the full temperature range. This indicates that at dilute doping, geometric effects dominate over thermal activation. **Intermediate Doping (1×10^{22} m^{-3})**: Planar φ_{max} increases from 0.35 V to 0.58 V (~66%), while radial structures increase from 0.42 V to 0.68 V (~62%). Radial junctions outperform planar ones by 15–20% at all temperatures, confirming the curvature-enhanced electrostatic confinement. **High Doping (1×10^{23} m^{-3})**: Planar junctions increase from 1.95 V to 2.85 V, a ~46% rise. Radial junctions grow from 2.45 V to 3.75 V, a ~53% enhancement. Crucially, radial junctions provide a consistent 25–32% higher φ_{max} than planar ones at equivalent doping and temperature, demonstrating their superior electrostatic robustness. **Temperature Effects**: The relative variation of φmax with temperature is minimal at low doping (<30% change), but becomes highly pronounced at higher doping levels (46–70% change). This confirms that incomplete ionization strongly amplifies thermal sensitivity in heavily doped junctions, with radial structures showing slightly stronger response than planar ones. **Device Implications**: The enhanced φ_{max} in radial junctions suggests improved charge separation, higher built-in barrier height, and stronger suppression of leakage currents compared to planar structures. At 1×10^{23} m^{-3} and 300 K, the radial φ_{max} (3.75 V) is 32% larger than the planar φ_{max} (2.85 V), which directly translates to higher breakdown thresholds and improved carrier confinement key for high-efficiency nanowire LEDs, photodetectors, and cryogenic solar cells. Conversely, planar junctions, with lower φ_{max} and wider depletion widths, may remain preferable in low-doping, low-field devices where carrier collection volume is more critical than electrostatic confinement.

In summary, the study demonstrates that radial p–n junctions consistently provide stronger electrostatic potentials (15–32% higher than planar), particularly at high doping and elevated temperatures, where incomplete ionization effects are significant. This geometry-driven advantage positions radial junctions as the preferred architecture for next-generation high-performance optoelectronic devices operating across wide thermal ranges, while planar junctions retain advantages in low-field, wide-depletion applications.

ORCID

Dildora A. Qalandarova, https://orcid.org/0009-0005-5130-464X;
Madinabonu Sh. Ibragimova, https://orcid.org/0009-0004-7867-7086
Jo‘shqin Sh. Abdullayev, https://orcid.org/0000-0001-6110-6616;
Ibrokhim B. Sapaev, https://orcid.org/0000-0003-2365-1554

REFERENCES

[1] D.L. Lepkowski, T.J. Garassman, J.T. Boyer, D.J. Chmielewski, C. Yi, M.K. Juhl, and S.A. Ringel, “23.4% monolithic epitaxial GaAsP/Si tandem solar cell,” Solar Energy Materials and Solar Cells, **230**, 111299 (2021). https://doi.org/10.1016/j.solmat.2021.111299
[2] G. Khudayberganov, and J.Sh. Abdullayev, “The boundary Morera theorem for domain τ^{+}(n-1),” Ufimsk. Mat. Zh. **13**(3), 196-210 (2021). http://dx.doi.org/10.13108/2021-13-3-191
[3] J.Sh. Abdullayev, U.S. Rakhmonov, N. Mahmudova, Orthonormal system for a matrix ball of the second type $B_{m,n}^{2}$ and its skeleton (Shilov's boundary) $X_{m,n}^{2}$,” Asia Pac. J. Math. **10**, 27 (2023). https://doi:10.28924/APJM/10-27
[4] S. Fan, Z.J. Yu, Y. Sun, W. Weigand, P. Dhingra, M. Kim, *et al.*, “20%-efficient epitaxial GaAsP/Si tandem solar cells,” Solar Energy Materials and Solar Cells, **202**, 110144 (2019). https://doi.org/10.1016/j.solmat.2019.110144
[5] M. Verma, S. Routray, G.S. Sahoo, and G.P. Mishra, “Bandgap engineered $GaAs_{0.95}P_{0.05}$ solar cell with double BSF,” Advanced Natural Sciences: Nanoscience and Nanotechnology, **14**(1), 015010 (2023). https://doi.org/10.1088/2043-6254/acb6e6
[6] M.Verma, S. Routray, G.S. Sahoo, and G.P. Mishra, “InP quantum well in p-i-n solar cell for sub-bandgap photon absorption,” Physica Scripta, **98**(7), 074004 (2023). https://doi.org/10.1088/1402-4896/ad00c6
[7] J.Sh. Abdullayev, I.B. Sapaev, J. Sh. Abdullayev, D.A. Juraev, M.J. Jalalov, and E.E. Elsayed, “Mathematical modeling of incomplete ionization in radial p-Si/n-GaAs heterojunctions: temperature and doping effects”, Journal of Electronic Materials, **54**, 10484–10492, (2025). https://doi.org/10.1007/s11664-025-12391-8
[8] D. Li, C. Luo, H. Wang, F. Ling, and J. Yao, “Active control of plasmon-induced transparency based on a GaAs/Si heterojunction in the terahertz range,” Optical Materials, **114**, 111609 (2021). https://doi.org/10.1016/j.optmat.2021.111609
[9] J.Sh. Abdullayev, and I.B. Sapaev, “Optimization of the influence of temperature on the electrical distribution of structures with radial p-n junction structures,” East European Journal of Physics, (3), 344–349 (2024). https://doi.org/10.26565/2312-4334-2024-3-39
[10] M.N. Hasan, Y. Zheng, J. Lai, E. Swinnich, O.G. Licata, M.A. Baboli, B. Mazumder, *et al.*, “Influences of native oxide on the properties of ultrathin Al_2O_3-interfaced Si/GaAs heterojunctions,” Advanced Materials Interfaces, **9**(13), 2101531 (2022). https://doi.org/10.1002/admi.202101531
[11] J.Sh. Abdullayev, and I.B. Sapaev, “Optimizing the Influence of Doping and Temperature on the Electrophysical Features of p-n and p-i-n Junction Structures,” Eurasian Physical Technical Journal, **21**(3(49)), 21–28 (2024). https://doi.org/10.31489/2024No3/21-28
[12] M. Jurisch, F. Börner, T. Bünger, S. Eichler, T. Flade, U. Kretzer, A. Köhler, *et al.*, “LEC- and VGF-growth of SI GaAs single crystals—Recent developments and current issues,” Journal of Crystal Growth, **275**(1–2), 283–291 (2005). https://doi.org/10.1016/j.jcrysgro.2004.10.092
[13] J.Sh. Abdullayev, I.B. Sapaev, and Kh.N. Juraev, “Theoretical analysis of incomplete ionization on the electrical behavior of radial p-n junction structures,” Low Temperature Physics, **51**, 60–64 (2025). https://doi.org/10.1063/10.0034646
[14] J.Sh. Abdullayev, and I.B. Sapaev, “Factors influencing the ideality factor of semiconductor p-n and p-i-n junction structures at cryogenic temperatures,” East European Journal of Physics, (4), 329–333 (2024). https://doi.org/10.26565/2312-4334-2024-4-37
[15] C.D. Thurmond, “The standard thermodynamic functions for the formation of electrons and holes in Ge, Si, GaAs, and GaP,” Journal of The Electrochemical Society, **122**(8), 1133 (1975). https://doi.org/10.1149/1.2134410
[16] J.Sh. Abdullayev, and I.B. Sapaev, “Modeling and calibration of electrical features of p-n junctions based on Si and GaAs,” Physical Sciences and Technology, **11**(3–4), 39–48 (2024). https://doi.org/10.26577/phst2024v11i2b05
[17] J. Herfort, H.-P. Schönherr, and K.H. Ploog, “Epitaxial growth of hybrid structures,” Applied Physics Letters, **83**(18), 3912–3914 (2003). https://doi.org/10.1063/1.1625426
[18] J.Sh. Abdullayev, “Influence of linear doping profiles on the electrophysical features of p-n junctions,” East European Journal of Physics, (1), 245–249 (2025). https://doi.org/10.26565/2312-4334-2025-1-26

[19] S. Heun, M. Sugiyama, S. Maeyama, Y. Watanabe, K. Wada, and M. Oshima, "Growth of Si on different GaAs surfaces: A comparative study," Physical Review B, **53**, 13534–13541 (1996). https://doi.org/10.1103/PhysRevB.53.13534

[20] P.K. Saxena, P. Srivastava, and A. Srivastava, "Defect analysis of MBE reactor-grown HgCdTe on Si, GaAs, GaSb, and CZT substrates through the TNL-Epigrow simulator," Journal of Electronic Materials, **53**, 5803–5812 (2024). https://doi.org/10.1007/s11664-024-11082-0

[21] A.B. Roy, N.H.R. Valiji, R. Mohammad, P. Giridhar, and P. Mondal, "Performance enhancement of Si/GaAs based heterojunction solar cells by opto-electronics modeling and optimization," in: *2024 International Conference on Recent Advances in Electrical, Electronics, Ubiquitous Communication, and Computational Intelligence (RAEEUCCI)*, (IEEE, 2024), pp. 1–6). https://doi.org/10.1109/RAEEUCCI61380.2024.10547792

[22] J.Sh. Abdullayev, and I.B. Sapaev, "Analytic analysis of the features of GaAs/Si radial heterojunctions: Influence of temperature and concentration," East European Journal of Physics, (1), 204–210 (2025). https://doi.org/10.26565/2312-4334-2025-1-21

[23] M. Piriyev, G. Loget, Y. Léger, L. Chen, A. Létoublon, T. Rohel, C. Levallois, *et al.*, "Dual bandgap operation of a GaAs/Si photoelectrode," Solar Energy Materials and Solar Cells, **251**, 112138 (2023). https://doi.org/10.1016/j.solmat.2022.112138

[24] J.Sh. Abdullayev, I.B. Sapaev, N. Esanmuradova, S. Kadirov, and S. Kuliyev, "Mathematical analysis of the features of radial p-n junction: Influence of temperature and concentration," East European Journal of Physics, (2), 220–225(2025). https://doi.org/10.26565/2312-4334-2025-2-24

[25] J. Alanis, S.J. Gutiérrez-Ojeda, R. Méndez-Camacho, and E. Cruz-Hernández, "Theoretical investigation of the growth of GaAs on Si(001), Si(110), Si(111), Si(113), and Si(331)," Surfaces and Interfaces, **44**, 103792 (2024). https://doi.org/10.1016/j.surfin.2023.103792

[26] R. Huang, Q. Wang, Y. Guo, and Z. Wang, "Comparative study on GaAs/Si heterojunction fabricated by nitrogen and oxygen plasma activated bonding," Vacuum, **208**, 111735 (2023). https://doi.org/10.1016/j.vacuum.2022.111735

[27] M. Yamaguchi, T. Takamoto, H. Juso, K. Nakamura, R. Ozaki, and N. Kojima, "33.7% efficiency Si tandem solar cell modules," in: *Proceedings of the 2024 IEEE 52nd Photovoltaic Specialist Conference (PVSC)*, (IEEE, 2024). https://doi.org/10.1109/PVSC57443.2024.10749502

[28] J.Sh. Abdullayev, K.Sh. Ruzmetov, Z.K. Matyakubov, "Carleman's Integral Formula in Cartesian Product of Matrix Upper Half-Plane," Azerbaijan Journal of Mathematics, 14(2), (2024). https://doi.org/10.59849/2218-6816.2024.2.36

[29] G. Khudayberganov, and J.Sh. Abdullayev, "Holomorphic continuation into a matrix ball of functions defined on a piece of its skeleton," Vestnik Udmurtskogo Universiteta. Matematika. Mekhanika. Komp'yuternye Nauki, **31**(2), 296–310 (2021). https://doi.org/10.35634/vm210210

[30] Khudayberganov, G.K., Abdullayev, J.S. & Rakhmonov, U.S. Functional Properties of the Bergman Kernel in the Space $C^n[m\times m]$," Lobachevskii J. Math. **46**, 1322–1335 (2025). https://doi.org/10.1134/S1995080225605247

[31] Jonibek Sh. Abdullayev, Gulmirza Kh. Khudayberganov, On the Blaschke matrix product and an analogue of the Horwitz-Rubel theorem for the Blaschke matrix product, Trans. Natl. Acad. Sci. Azerb. Ser. Phys.-Tech. Math. Sci. Mathematics, **45**(4), 3-19 (2025). https://doi.org/10.30546/2617-7900.45.4.2025.019

[32] J.Sh. Abdullayev, I.B. Sapaev, and S.R. Kadirov, "The role of recombination types in efficiency limits of radial p-n junctions based on Si and GaAs," East European Journal of Physics, (2), 252–257 (2025). https://doi.org/10.26565/2312-4334-2025-2-30

[33] M. Haris, S.A. Loan, and Mainuddin, "Si/GaAs hetero junction tunnel FET: Design and investigation," Journal of Nanoelectronics and Optoelectronics," **14**(10), 1434–1444 (2019). https://doi.org/10.1166/jno.2019.2575

[34] J. Liang, T. Miyazaki, M. Morimoto, S. Nishida, N. Watanabe, and N. Shigekawa, "Electrical properties of p-Si/n-GaAs heterojunctions by using surface-activated bonding," Applied Physics Express, **6**(2), 021801 (2013). https://doi.org/10.7567/APEX.6.021801

[35] J. Sh. Abdullayev, Abdullayeva, L., Agamalieva, L., & Ismailova, R. (2025). Correlating Ni microstructure with Schottky barrier homogeneity in monolayer MoS_2 field-effect transistors. Advanced Physical Research, 7(3), 350–357. https://doi.org/10.62476/apr.73350

[36] Abdullayev, J. S., Sapaev, I. B., Kadirov, S. R., & Abdullayev, J. Sh. "Modeling of optoelectronic properties in pSi/n-$Cd_mZn_{1-m}S$ heterojunctions: Effects of composition and temperature," Journal of Electronic Materials, **54**(10), 11607–11617 (2025). https://doi.org/10.1007/s11664-025-12480-8

[37] I.B. Sapaev, J.I. Razzokov, J.S. Abdullayev, D.A. Qalandarova, and M.S. Ibragimova, "Bandgap-Engineered pSi/n-Cd_xS_{1-x} Heterojunctions: Effect of Composition on Optoelectronic Behavior," East European Journal of Physics, (4), 442-448 (2025). https://doi.org/10.26565/2312-4334-2025-4-44

[38] S. Strzelecka, M. Pawlowska, A. Hruban, M. Gladysz, E. Wegner, A. Gladki, and W. Orlowski, "Investigation of As-precipitates in SI GaAs," in: *Solid State Crystals: Growth and Characterization*, edited by J. Zmija, A. Majchrowski, J. Rutkowski, and J. Zielinski, vol. 3178, (SPIE, 1997), pp. 238–241. https://doi.org/10.1117/12.280741

[39] T. Yu, H. Zhang, D. Li, and Y. Lu, "Electronic and optical properties of silicene on GaAs(111) with hydrogen intercalation: A first-principles study," RSC Advances, **11**, 16040–16050 (2021). https://doi.org/10.1039/D1RA01959G

[40] I. Sapaev, B. Sapaev, D. Abdullaev, J. Abdullayev, A. Umarov, R. Siddikov, A. Mamasoliev, and K. Daliev, "Influence of the parameters to transition capacitance at NCDS-PSI heterostructure," E3S Web of Conferences, **383**(04022), 1–7 (2023). https://doi.org/10.1051/e3sconf/202338304022

[41] A.A. Sushkov, D.A. Pavlov, A.I. Andrianov, V.G. Shengurov, S.A. Denisov, V.Y. Chalkov, R.N. Kriukov, *et al.*, "Comparison of III–V heterostructures grown on Ge/Si, Ge/SOI, and GaAs," Semiconductors, **56**, 122–133 (2022). https://doi.org/10.1134/S106378262201012X

[42] R. Huang, Z. Wang, K. Wu, H. Xu, Q. Wang, and Y. Guo, "Hybrid bonding of GaAs and Si wafers at low temperature by Ar plasma activation," Journal of Semiconductors, **45**(4), 042701 (2024). https://doi.org/10.1088/1674-4926/45/4/042701

[43] B. Abdullaev, and D. Qalandarova, "The classes of $(A)sh_m$ and $(B)sh_m$ functions," Annales Polonici Mathematici, **132**, 101-108 (2024). https://doi.org/10.4064/ap230727-30-11

[44] J.Sh. Abdullayev, "An analogue of Bremermann's theorem on finding the Bergman kernel for the Cartesian product of the classical domains $\mathfrak{R}_{II}(m,k)$ and $\mathfrak{R}_{I}(n)$," Bul. Acad. Ştiinţe Repub. Mold. Mat. (3), 88–96 (2020).

[45] U.S. Rakhmonov, J.Sh. Abdullayev, “On properties of the second type matrix ball $B_{m,n}^2$ from space $C^n[m\times m]$,” J. Sib. Fed. Univ. Math. Phys. **15**(3), 329–342 (2022). https://doi.org/10.17516/1997-1397-2022-15-3-329-342

[46] J. Sh. Abdullayev, “Estimates the Bergman kernel for classical domains É. Cartan's,” Chebyshevskii Sb. **22**(3), 20–31 (2021). https://doi.org/10.22405/2226-8383-2018-22-3-20-31

[47] Bebitov, R., Abdulkhaev, O., Yodgorova, D., Istamov, D., Khamdamov, G., Kuliyev, S., Abdullaev, J. Sh., Khakimov, A., & Rakhmatov, A. (2023). Potential distribution over temperature sensors of p-n junction diodes with arbitrary doping of the base region. *E3S Web of Conferences, 401,* 03062. https://doi.org/10.1051/e3sconf/202340103062

[48] Abdullayev, J.S., Qalandarova, D.A., Ibragimova, M.S. et al. Experimental and Simulation-Based Investigation of p-Si/n-CdS Heterojunctions: From Cryogenic Freeze-Out to Room Temperature Operation. J. Electron. Mater. **55**, 2229–2239 (2026). https://doi.org/10.1007/s11664-025-12642-8

[49] M. Akhmedov, *et al*. “Picosecond-pulsed laser ablation of aluminum foils: crater morphology and plasma parameters,” Engineering Research Express, **7**(3), 035362 (2025). https://doi.org/10.1088/2631-8695/ae0092

МАТЕМАТИЧНЕ МОДЕЛЮВАННЯ ЕЛЕКТРОСТАТИЧНОГО ПОТЕНЦІАЛУ В РАДІАЛЬНИХ І ПЛАНАРНИХ p-n ПЕРЕХОДАХ: ПОРІВНЯЛЬНЕ ДОСЛІДЖЕННЯ

Дільдора А. Каландарова[1], Мадінабону Ш. Ібрагімова[1], Джошкін Ш. Абдуллаєв[2], Іброхім Б. Сапаєв[2,3,4,5]
[1]Ургенчський державний університет, вулиця Хаміда Олімджона, 14, Ургенч, 220100 Узбекистан
[2]Національний дослідницький університет ТІІАМ, кафедра фізики та хімії, Ташкент, Узбекистан
[3]Західно-Каспійський університет, Баку, Азербайджан
[4]Ташкентський університет прикладних наук, вулиця Університетська, 28, Ташкент 100095, Узбекистан
[5]Інженерний факультет, Центральноазіатський університет, Ташкент 111221, Узбекистан

Ця робота представляє комплексне математичне та чисельне дослідження електростатичного потенціалу в планарних та радіальних кремнієвих *p–n* переходах з урахуванням взаємодії геометрії пристрою, температури та неповної іонізації легуючих домішок. Розроблено самозгідне двовимірне рішення рівняння Пуассона у декартовій та циліндричній системах координат, з явним урахуванням неповної іонізації за статистикою Фермі–Дірака в діапазоні 50–300 K. При 100 K неповна іонізація зменшує ефективну густину просторового заряду на 38–45%, збільшує ширину збідненої області на 55–70% та змінює вбудований потенціал до 42% порівняно з прогнозами при кімнатній температурі. Радіальні переходи демонструють сильну локалізацію електричного поля через кривизну, забезпечуючи 15–32% вищий максимальний потенціал, ніж у планарних переходів за тих самих умов легування та температури. Для $N = 10^{23}$ м$^{-3}$ максимальний потенціал зростає з 1.95 → 2.85 В (планарний) та 2.45 → 3.75 В (радіальний) у діапазоні 100–300 K, що відповідає зростанню на 46% та 53% відповідно. Пікові значення електричного поля досягають 3.2×10^6 В·м$^{-1}$, при цьому радіальні переходи перевищують планарні на ~7-12%, демонструючи стабільно 25–32% сильніше електростатичне обмеження. Ці результати кількісно демонструють, що геометрія, легування та неповна іонізація спільно визначають електростатику переходів. Радіальні *p–n* переходи забезпечують вищу електростатичну ефективність, що робить їх ідеальними для високоефективних нанодротяних діодів, кріогенних фотодетекторів та сучасних оптоелектронних пристроїв.

Ключові слова: *радіальний p–n перехід; планарний p–n перехід; рівняння Пуассона; моделювання електростатичного потенціалу; неповна іонізація; імовірність іонізації; циліндрична система координат; низькотемпературні ефекти*